

Controlled Individual Skyrmion Nucleation at Artificial Defects Formed by Ion Irradiation

Kayla Fallon, Sean Hughes, Katharina Zeissler, William Legrand, Fernando Ajejas, Davide Maccariello, Samuel McFadzean, William Smith, Damien McGrouther, Sophie Collin, Nicolas Reyren, Vincent Cros, Christopher H. Marrows, and Stephen McVitie*

Magnetic skyrmions are particle-like deformations in a magnetic texture. They have great potential as information carriers in spintronic devices because of their interesting topological properties and favorable motion under spin currents. A new method of nucleating skyrmions at nanoscale defect sites, created in a controlled manner with focused ion beam irradiation, in polycrystalline magnetic multilayer samples with an interfacial Dzyaloshinskii–Moriya interaction, is reported. This new method has three notable advantages: 1) localization of nucleation; 2) stability over a larger range of external field strengths, including stability at zero field; and 3) existence of skyrmions in material systems where, prior to defect fabrication, skyrmions were not previously obtained by field cycling. Additionally, it is observed that the size of defect nucleated skyrmions is uninfluenced by the defect itself—provided that the artificial defects are controlled to be smaller than the inherent skyrmion size. All of these characteristics are expected to be useful toward the goal of realizing a skyrmion-based spintronic device. This phenomenon is studied with a range of transmission electron microscopy techniques to probe quantitatively the magnetic behavior at the defects with applied field and correlate this with the structural impact of the defects.

1. Introduction

A magnetic skyrmion is a quasiparticle of magnetization characterized by its non-trivial topology. They appear in systems with a Dzyaloshinskii–Moriya interaction (DMI)—which occurs in magnetic systems lacking structural inversion symmetry.^[1,2] Skyrmions were first observed in lattice form in helimagnets with cubic but non-centrosymmetric crystal structures (such as the B20 crystals MnSi and FeCoSi^[3,4]). They were found to be great candidates for low energy spintronic devices owing to their small size, stability, and high mobility under spin-polarized currents.^[5,6] Recent research efforts have centered on finding a material system capable of nucleating individual skyrmions at room temperature and low magnetic fields with the aim of realizing a skyrmion-based spintronic device.

DMI is also present at the interface between a ferromagnet and a heavy metal—where the interface itself breaks the inversion symmetry.^[7–9] Both isolated skyrmions^[10] and skyrmion lattices^[8] have been observed experimentally in interface-driven systems. Pt/Co/Ir is a good example of an interface system where the DMI can reach the high value of 2 mJ m⁻², here the asymmetric heavy metal interfaces either side of the magnetic material serve to effectively boost the DMI.^[11–13] This type of interfacial DMI—which enables the use of polycrystalline materials—allows for easily-deposited, tunable DMI systems in which skyrmions have been observed at room temperature.^[12,14–18]

One crucial step necessary for realizing a skyrmion-based device lies in finding a reliable and controllable method of nucleating individual skyrmions. A multitude of nucleation methods have been proposed in recent years and these can be put into three categories based on: electrical currents,^[10,19–24] laser pulses,^[25–27] and locally applied electric fields.^[28,29] Skyrmions can also nucleate at naturally occurring defects in the material;^[30,31] theoretical studies, which consider nonmagnetic defects, find that defects both localize skyrmion nucleation and reduce the nucleation energy barrier.^[32,33] However, because of their random location and variable character, naturally occurring defects offer little control over the formation of skyrmions and are unsuitable as a nucleation method for devices.

Dr. K. Fallon, S. Hughes, Dr. S. McFadzean, W. Smith,
Dr. D. McGrouther, Prof. S. McVitie
SUPA School of Physics and Astronomy
University of Glasgow
Glasgow G12 8QQ, UK
E-mail: Stephen.McVitie@glasgow.ac.uk

Dr. K. Zeissler, Prof. C. H. Marrows
School of Physics and Astronomy
University of Leeds
Leeds LS2 9JT, UK


Dr. W. Legrand, Dr. F. Ajejas, Dr. D. Maccariello, Dr. S. Collin,
Dr. N. Reyren, Dr. V. Cros
Unité Mixte de Physique
CNRS
Thales

Univ. Paris-Sud
Université Paris-Saclay
Palaiseau 91767, France

Dr. K. Zeissler
National Physical Laboratory
Hampton Road, Teddington TW11 0LW, UK

© 2020 The Authors. Published by WILEY-VCH Verlag GmbH & Co. KGaA, Weinheim. This is an open access article under the terms of the Creative Commons Attribution License, which permits use, distribution and reproduction in any medium, provided the original work is properly cited.

The copyright line for this article was changed on 2 April 2020 after original online publication.

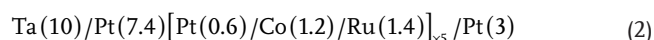
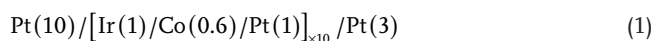
 The ORCID identification number(s) for the author(s) of this article can be found under <https://doi.org/10.1002/smll.201907450>.

DOI: 10.1002/smll.201907450

In this paper, we propose an original method of nucleating skyrmions using a focused ion beam (FIB) microscope to create nanoscale artificial defects. In Pt/Co based multilayers, ion irradiation is well-documented to both reduce the perpendicular anisotropy and increase the coercivity in a dose-dependent manner.^[34–38] These effects have been exploited to engineer or tailor the local behavior of magnetic systems.^[39–41] For example a study found that extended circular areas of FIB irradiation (diameter 300 nm to 1 μm) in multilayers of Pt/Co can stabilize anti-skyrmions and Bloch skyrmions.^[41] In contrast to the aforementioned study, here we propose point-like FIB-induced defects to nucleate Néel-type skyrmions.

2. Results

To explore artificial defects as a mechanism for skyrmion nucleation, point-like defects were created on two distinct multilayered Pt/Co based systems. As will be demonstrated shortly, in their “as-deposited” state, one of these samples has a high magnetic remanence (close to M_s) and supports both isolated skyrmions and Néel-type walls where the other has a low magnetic remanence (close to zero) and supports only Néel walls (in the field-driven regime). Both samples were prepared by dc magnetron sputtering and the layer structure is outlined in the following list, where the bracketed numbers are the layer thicknesses in nm and the subscript number is the number of repeat layers



Studying two samples with slightly different layer composition and magnetic behavior provides a useful test of the reproducibility of this nucleation method while also demonstrating the sensitivity of the method to the multilayer structure.

For transmission electron microscopy (TEM) studies the samples were deposited on substrates with an electron transparent Si_3N_4 window suspended from a thicker Si frame. Alternating gradient field magnetometry confirms all samples to support magnetization out of the sample plane, as is promoted by the interface-induced perpendicular magnetic anisotropy (PMA).^[42] Artificial defects were made with a FEI Nova NanoLab 200 scanning electron microscope (SEM) and FIB. The samples were studied using a JEOL ARM200cF TEM, optimized for magnetic imaging, operated at 200 kV.^[43] In situ magnetizing experiments were performed (at room temperature) on samples 1 and 2 using the Fresnel mode of Lorentz TEM to explore the behavior of the samples with applied field before and after defect creation. Details of the magnetic textures at the defects in sample 1 were studied with quantitative, high resolution differential phase contrast (DPC) images. For multilayer materials with PMA, DPC imaging is enabled through advanced processing allowed by pixelated detectors^[44–46]—this work uses the Medipix3 hybrid pixelated detector, with a Merlin readout system, from Quantum Detectors Ltd. We also explore the structural impact of the defects both in plan-view with bright field (BF) images and in cross-section with high angle annular

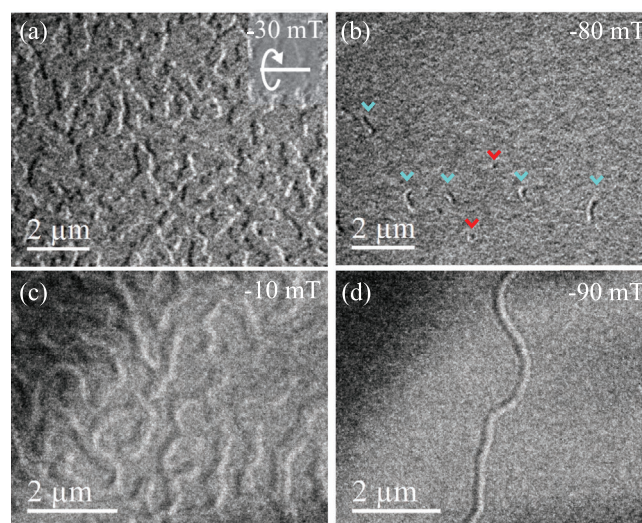


Figure 1. Fresnel images of sample 1 (tilted 20° about axis labeled) and 2 (tilt provided by surface contortion) in the as-grown state. For sample 1, the labyrinth-like state a) must be passed to obtain skyrmions (mean diameter ≈ 150 nm) at a higher field b) before saturation. The skyrmions are sparse and where present are highlighted by a red arrow above the skyrmion. c) Sample 2 also has a labyrinth-like coercive state. d) Upon increasing the field strength toward saturation, the domains become sparse and thread-like, with pairs of domain walls separated by ≈ 150 nm. No skyrmions are observed as the external field strength is increased and the sample saturates.

dark field (HAADF) images taken from sample 1. The different TEM imaging modes will be discussed later in the paper.

In **Figure 1**, we show snapshots of the behavior representative of samples 1 and 2 (unmodified by FIB) in an out-of-plane applied magnetic field in a series of Fresnel images. In the Fresnel mode of Lorentz TEM, magnetic contrast is visible as either bright or dark lines at the position of domain walls. For these samples with PMA and Néel-type walls the sample must be tilted to get contrast from the out of plane domains.^[45–47] Néel-type skyrmions in particular are visible in Fresnel images as dot-like objects with contrast which is dark on one side and bright on the other. The electron transparent window on sample 2 is significantly buckled, this surface contortion provides local tilt when the sample is notionally “untilted” with respect to the thicker flat Si frame as detailed previously.^[46] For example in **Figure 1a,b** from sample 1 (flat surface), contrast is provided by tilting the sample 20° with respect to the sample plane. Conversely **Figure 1c,d** from sample 2 (buckled surface), were acquired with no explicit sample tilt but the images show clear magnetic contrast indicative of local film tilting. In the TEM we perform in situ magnetizing experiments using the objective lens of the microscope, which allows application of an out of plane field variable between 10 mT (the remanent field of the lens) and 2 T. Fields below the remanent value must be set individually using specialized hardware external to the TEM.

We first discuss details of the field-driven magnetization reversal, highlighting the possible existence of stable isolated skyrmions. Previous work has shown that the stability of isolated skyrmions is generally restricted at low-fields by elliptical instabilities, where the skyrmion is unstable and expands into a larger magnetic object lacking circular symmetry.^[48,49] As the

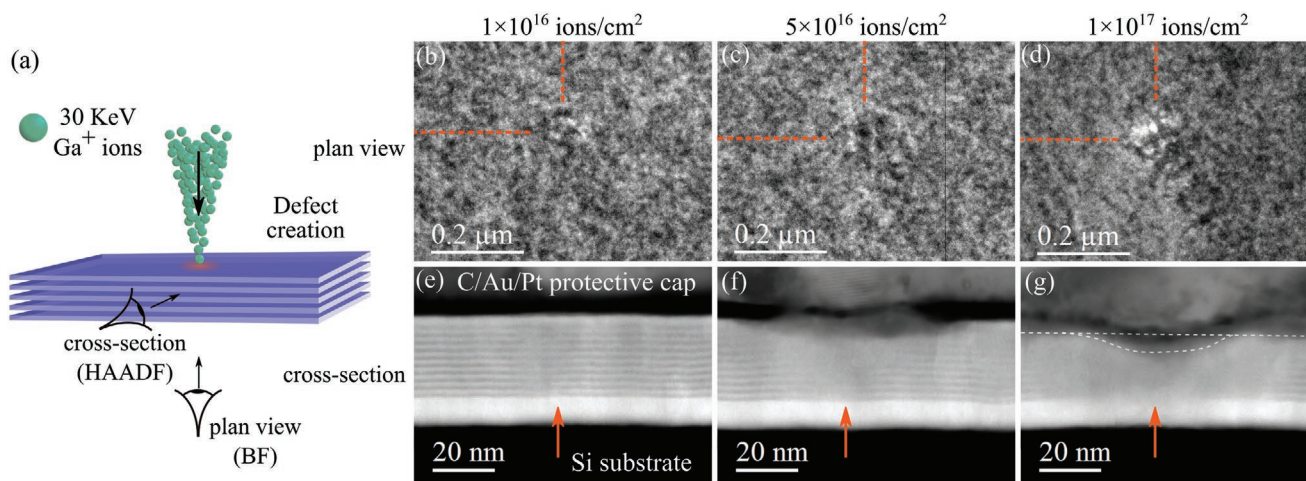


Figure 2. a) Schematic of FIB defect creation. Bright field (BF) images of the defects in plan view—b–d) looking straight down on the sample and high angle annular dark field (HAADF) images of the defects in cross-section. e–g) The gradual erasing of the layer structure with increasing ion dose can be seen in HAADF images—at 10^{16} ions per cm^2 the layer structure is mostly undisturbed, at 5×10^{16} ions per cm^2 there is a shallow “u” shape with clear intermixing and at 10^{17} ions per cm^2 there is slight milling (highlighted by the white dashed lines) and no layer details remaining. b–d) The corresponding changes to the grain structure are seen in BF images. All images taken on sample 1 and the arrows on HAADF images and lines on BF images are to guide the eye to the center of the defect.

field strength is increased these objects contract into compact circularly symmetric skyrmions, which reduce in radius as the field strength is further increased^[48,50] before becoming radially unstable at a critical external field strength.^[48,49] At this point the skyrmions radius rapidly shrinks until the skyrmion annihilates by collapsing into itself.^[33] The Fresnel images in Figure 1 show discrete points in the reversal of the magnetization from saturation in an out-of-plane positive field to saturation in a negative field for both samples. Prior to defect fabrication, sample 1 exhibits the behavior outlined above. At low external field strengths, the sample supports a labyrinth-like coercive state (see Figure 1a). Skyrmions are first stabilized in an applied field of -50 mT with a mean diameter of 170 ± 20 nm, decreasing to 150 ± 20 nm in a -80 mT field. Figure 1b is annotated to highlight the presence of both skyrmions (red arrows) and expanded domains (cyan arrows) which are skyrmion-like objects that are elongated due to the aforementioned elliptical instability. Note, that the skyrmion diameter can be quantitatively measured from Fresnel images as the difference in the position of the extremes of bright and dark contrast—this property is unaffected by the image defocus (≈ 10 mm here). By -90 mT the skyrmions are annihilated and the sample saturated. Sample 1 has a high magnetic remanence—upon increasing the applied field from negative saturation toward positive saturation, no domains form until the sample is in a field of $+20$ mT. Without defects, skyrmions are not observed in sample 2. It also has a dense labyrinth-like coercive state, Figure 1c, but as the field strength is increased the domains shrink to sparse thread-like objects with long domain walls pairs separated by ≈ 150 nm, Figure 1d. By -100 mT the sample has saturated with no intermediate skyrmion state observed. Sample 2 has a magnetic remanence of almost zero: when the field is increased again toward positive saturation, domains begin to form just before -10 mT.

As discussed earlier, FIB irradiation can alter the magnetic and structural properties of magnetic multilayer films. To

explore this effect for skyrmion nucleation, FIB defects were made using a FEI Nova NanoLab 200 SEM and FIB with a 30 keV Ga^+ beam energy and beam current of 10 pA—giving an ion beam diameter of 10 nm. This diameter is defined as the probe full width half maximum (FWHM), but the probe has extensive tails over a larger distance leading to FIB defined features larger than the quoted beam diameter.^[40] A wide range of defects were made on sample 1 with the geometry shown in Figure 2a with the beam normal to the sample surface. The irradiation was controlled to deliver a dose between 10^{14} and 10^{18} ions per cm^2 . To precisely control the ion dose (and to fabricate the smallest possible defects) direct machine commands were used to irradiate precisely one spot of the sample with the ion beam. More technical details related to the creation of point-like FIB defects are provided in the supporting information.

The structural impact of the defects on sample 1 has been studied in both plan view, with BF images, and in cross-section, with HAADF images. For the plan view study, spot defects were made on sample 1. Conversely, for the cross-sectional study, line defects (of equivalent dose to the spot defects) were made on the thicker Si frame of sample 1. A cross-sectional electron transparent lamella was prepared from this region using a Xe^+ plasma FIB. To protect the sample from damage during the fabrication process, the region was first coated with carbonaceous platinum.

A selection of BF and HAADF images from defect sites created with different ion dose are shown in Figure 2. The top row of Figure 2 shows the BF images in which the granular structure of the polycrystalline sample is visible. The bottom row shows the HAADF images in which the discrete layer structure of the sample is visible. HAADF imaging is essentially atomic number Z imaging, where brighter image contrast corresponds to a higher Z material, hence in these images, in the area corresponding to the multilayer, Ir and Pt are bright ($Z = 77, 78$ respectively) and Co is dark ($Z = 27$). A defect of dose

1×10^{16} ions per cm^2 is shown in the first column of images, Figure 2b,e. There is little evidence of damage from this defect in the HAADF image, with each layer of the structure resolvable, similarly the center of the BF image shows some slight grain enlargement—a known effect of ion irradiation on polycrystalline films^[51]—but no grain growth out with the normal distribution of sizes. The 5×10^{16} ions per cm^2 defect causes visible damage to the layer structure, Figure 2f: there is intermixing of the layers in a “u”-shape extending across a distance of 70 nm in the top layers and to a depth of up to ≈ 7 layers at the center of the defect. Intermixing is identified by loss of the black/white alternating layer contrast. The corresponding BF image shows similar grain growth to the 1×10^{16} ions per cm^2 defect. There is a considerable area of grain enlargement associated with the 1×10^{17} ions per cm^2 defect, Figure 2g, and the layer structure has been erased over a distance of 80 nm—additionally this defect causes milling of 6–7 nm into the sample, judging by the infill of the protective layers as marked by the white dashed line overlaid on Figure 2g. It is noted that defects smaller than 10^{16} ions per cm^2 show no visible signs of damage when judged by the grain size and the uniformity of the layer structure. Defects created with doses larger than 10^{18} ions per cm^2 resulted in clearly defined holes through the multilayer stack due to milling.

Figure 3a shows a Fresnel image of sample 1, patterned with an array of ≈ 250 nm diameter defects (ion dose 10^{17} ions per cm^2).

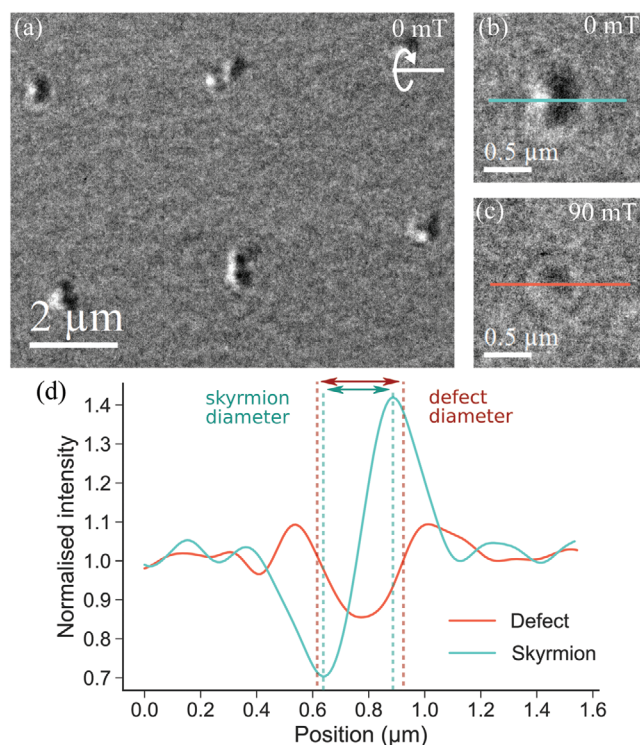


Figure 3. a) Fresnel image of sample 1 after creation of extended defects with ion dose 10^{17} ions per cm^2 in a field free environment—skyrmions are clearly visible at most defect sites. b) Enlarged image of a defect with skyrmion for comparison with c) enlarged image of a saturated defect. d) Line trace indicates that the distinction between a skyrmion and defect is easily made. All Fresnel images taken with sample tilt of 20° about the axis indicated.

The image was acquired in a zero-field environment at room temperature after application of a saturating field. Strikingly, single skyrmions can be observed at many of the defect sites. Compared to the spot defects in Figure 3 these are extended defects (created with a different method as explained in the FIB patterning section of the Supporting Information), purposed in this section for two reasons: to demonstrate the separation of nonmagnetic defect contrast and magnetic skyrmion contrast; and to evaluate the relationship between defect size and skyrmion size.

Figure 3b,c illustrates the contrast from the top left defect site in (a) with and without a skyrmion respectively. The changed physical structure of the defect results in nonmagnetic image contrast even after the skyrmion has been removed (by saturating the defect site) as shown in Figure 3c. The line traces taken from the defects are shown in Figure 3d. These indicate that the contrast from a saturated defect site is symmetric compared to a defect site with a skyrmion. Moreover, the magnetic contrast in these images is generated by the sample tilt (here $+20^\circ$), hence any magnetic contrast will reverse with tilt, i.e., at -20° black becomes white and vice versa. Hence, these differences in contrast allow defects and skyrmions to be easily distinguished from one another. Also indicated on Figure 3d is the defect diameter and the skyrmion diameter. As mentioned above, the mean defect diameter (averaged over multiple defect sites) is 250 ± 30 nm while the mean skyrmion diameter (in zero field) is 300 ± 10 nm. The similarity between the defect size and skyrmion size suggests that the skyrmion size could be linked to the defect size. For defects smaller than the “natural” skyrmion size we observe a different relationship, but we discuss this in detail later.

To be technologically advantageous the defects should cause a minimal increase to the depinning current required to move a skyrmion from the defect site. Whilst this is not studied here directly, it is known that local changes in anisotropy increase the pinning field,^[23] and that higher ion doses cause a larger modification of the anisotropy.^[34–38] Hence, we determine the lowest dose required to cause low-field, room-temperature nucleation for samples 1 and 2. The enlargement of the grains is thought less likely to be problematic as a previous study identifies the most severe pinning for grain sizes which are the same size as the skyrmions^[23] and the FIB enlarged grains are still an order of magnitude smaller than the skyrmions.

Sample 1 was irradiated with ten different doses between 10^{14} and 10^{18} ions per cm^2 , with five repetitions of each. Similarly, sample 2 was irradiated with doses between 10^{12} and 10^{16} ions per cm^2 . These were spot defects created by irradiating precisely one position on the sample with the FIB probe. The charts in Figure 4 summarize the field behavior of the magnetization at each type of defect site on a) sample 1 and b) sample 2. Note that on Figure 4a, the field scale is not linear between ± 10.8 mT as the objective lens field cannot be varied smoothly between these values. Doses below 5×10^{16} ions per cm^2 on sample 1 and below 5×10^{15} ions per cm^2 on sample 2 showed no nucleation activity and are not included in the charts. The lightest color indicates that all defect sites of a given dose are unchanged from a magnetically saturated state, while the darkest color indicates that all defect sites of a given dose have a magnetic object local to the defect. The icon inset on each square

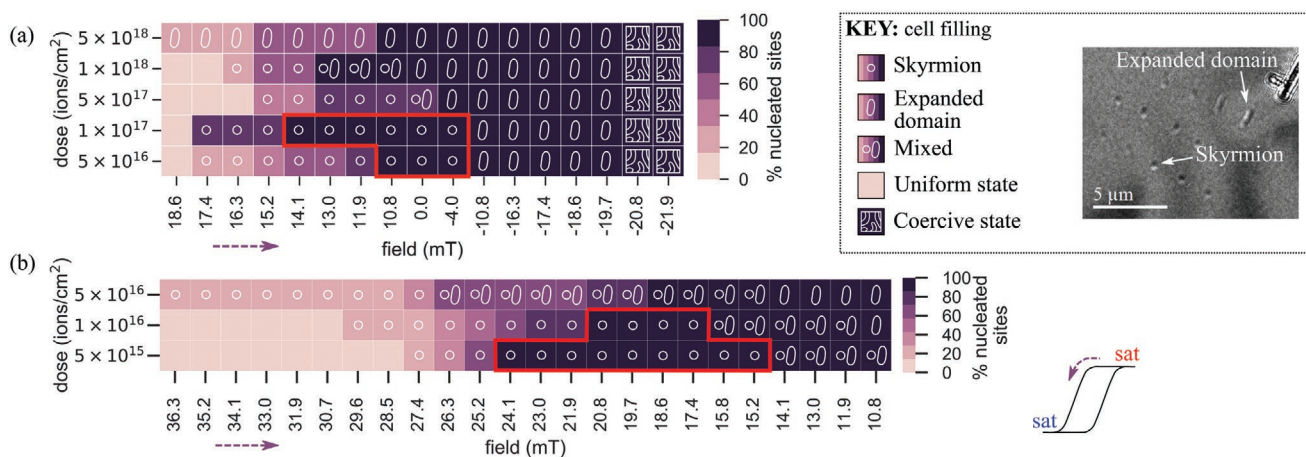


Figure 4. Charts presenting the detailed behavior of defect sites as a function of ion dose and applied out of plane field on a) sample 1 and b) sample 2. These charts are explained by the colorbar and key. The Fresnel image, from sample 2, provides examples of the different magnetic states in the key. Squares outlined in red highlight the most interesting parts of the chart that have 100% skyrmion nucleation.

indicates the nature of the magnetic object local to the defect: a circle indicates all occupied sites have skyrmions; a bean shape indicates all occupied sites have expanded domains; both a circle and bean indicate a mixture of the above; and the maze icon indicates the sample is in a state close to remanence with labyrinth domains (as in Figure 1a,c) where it is meaningless to evaluate the behavior local to the defect sites. As described earlier, the term “expanded domain” refers to an extended noncircular magnetic object, only compact circular magnetic objects have been identified as skyrmions—examples of both are marked in the Fresnel image in Figure 4. Hence the areas of most interest (outlined in red) are those with a circle on a dark background, indicating all defect sites with that dose have stabilized skyrmions, i.e., 100% success rate of skyrmion nucleation.

The behavior of the samples was again monitored as the applied field was lowered from saturation in a positive out of plane field to saturation in a negative field. Nonlocal to defect sites the magnetic reversal is the same as in the unmodified samples as discussed in relation to Figure 1. However, as highlighted in red, both samples have specific combinations of applied field and defect dose that cause local nucleation and retention of compact individual skyrmions at 100% of defect sites. Table 1 provides details of the “ideal” artificial defects found to cause 100% skyrmion nucleation in samples 1 and 2.

Critically, for sample 1 the field range of skyrmion stability includes zero applied field. Sample 2 exhibited very similar behavior with dose and field to sample 1 although, as expected

Table 1. Summary of artificial defect types that cause 100% skyrmion nucleation at room temperature—detailed is the dose associated with each successful defect and field range over which the nucleated skyrmions remain stable.

Sample	Defect dose [ions per cm ²]	Range of stability [mT]
1	5×10^{16}	+10.8 to -4.0
1	1×10^{17}	+14.1 to -4.0
2	5×10^{15}	+24.1 to +15.8
2	1×10^{16}	+20.8 to +17.4

from a low magnetic remanence system, to retain compact skyrmions a bias field was required. This is a particularly interesting result as skyrmions were not observed at room temperature in sample 2 prior to defect creation. Furthermore, the dose required to nucleate skyrmions is an order of magnitude smaller for sample 2 compared to sample 1—demonstrating the extreme sensitivity of this nucleation method to the sample structure. As seen in the cross-sectional images presented in Figure 2f,g, the energy imparted in the sample by the ions causes damage and intermixing of the multilayer structure: alloying the multilayer. Given the different elemental composition of the two multilayer stacks studied, the magnetic properties of the resulting alloy are certainly different. For example, an older study^[52] characterizes the magnetization of binary alloys of Co and various transition metals. It shows that the magnetization of Co is more sensitive to alloying with Ru than either Ir or Pt—giving a possible explanation for the greater sensitivity of sample 2 to ion dose than sample 1.

From the spot defects on sample 1, the mean skyrmion size in zero field is 170 ± 30 nm at 5×10^{16} ions per cm² defects and 180 ± 30 nm at 1×10^{17} ions per cm² defects (details of these measurements are in the supporting information). From the structural imaging in Figure 2, on sample 1 these defects are associated with an area of damage around 100 nm in diameter. This is in stark contrast to the extended 250 nm diameter defects that nucleate 300 nm diameter skyrmions presented in Figure 3.

The defect nucleated skyrmions in sample 2 are around 300 nm in diameter. As no skyrmions were observed in sample 2 without defects there can be no direct comparison—however it is useful to consider the large difference in diameter of skyrmions measured from sample 2 compared to sample 1. The images of defects made on sample 2 show no visible non-magnetic phase contrast, like presented in the Fresnel image in Figure 3c, or obvious grain growth, like shown in the BF images in Figure 2b–d. Consequently, although not measured, the lateral size of the defects is almost certainly smaller than measured for sample 1 but the skyrmions are larger.

This information leads us to the conclusion that, for defects smaller than the “natural” skyrmion size, the size of the defect

nucleated skyrmions is determined by the sample properties and not the defect itself. The skyrmion size data relating to sample 1 (both unmodified and with artificial defects) and sample 2 is provided in full in the Supporting Information.

DPC images were taken of sample 1, and allow quantitative measurement of the saturation induction B_s of the film near a defect, where $B_s = \mu_0 M_s$. DPC is a scanning TEM (STEM) technique where the Lorentz deflections of the electron beam are measured directly by measuring shifts in the unscattered central diffraction disk. For skyrmionic multilayer materials, DPC datasets must be acquired using a pixelated detector. The combination of perpendicular magnetization (the samples must be tilted in order to cause any beam deflection) and large sample thickness compared to the active magnetic thickness mean these materials cause only a small beam deflection but generate considerable, undesirable diffraction contrast associated with the crystallites. This diffraction contrast completely masks the magnetic contrast in standard DPC, however, the more advanced processing enabled by pixelated detectors can reduce this contrast and allow for successful quantitative imaging with DPC.^[44–46]

As outlined in existing studies,^[45,46] the beam Lorentz deflection angle β from perpendicularly magnetized materials depends on the sample tilt and is proportional to B_s . **Figure 5a** shows a DPC image from a 5×10^{16} ions per cm^2 defect site on sample 1 in a field of 10 mT. The contrast is from the magnetic induction associated with a circular skyrmion which is tilted with respect to the electron beam. The skyrmion is then imaged as an extended dipolar field. The light central area of **Figure 5a** shows where this dipolar field is strongest, and the width of this bright area (taken parallel to the tilt axis) corresponds to the diameter of the skyrmion, measured to be 150 nm. Diagrammatic descriptions are provided in the Supporting Information to aid interpretation of DPC images of Néel skyrmions. A white circle, diameter 70 nm, is overlaid at the position of the defect with size matching the area of physical damage associated with this dose, as identified from **Figure 2f**. The resolution of DPC imaging allows us to observe

that the skyrmion is situated with its wall located on the defect. This is in good correlation with a theoretical paper which, in a study of isolated skyrmions at nonmagnetic defects, observes the same behavior in simulation.^[33] A line trace, averaged over 15 pixels, was taken from the area marked in **Figure 5a**, near to the defect, and is shown next to the DPC image. By fitting a hyperbolic tangent function to this line trace, the deflection due to the domains was determined as $1.7 \pm 0.2 \mu\text{rad}$ (sample was tilted by 24.6°). From this B_s was calculated to be 1.2 ± 0.1 T, assuming a total magnetic thickness of 6 nm resulting from ten 0.6 nm thick Co layers. This is compared to magnetometry measurements from this sample before irradiation which measured M_s as $1.0 \pm 0.1 \text{ MA m}^{-1}$ —equivalent to 1.2 ± 0.1 T. This quantitative analysis suggests that the defect has caused skyrmion nucleation in all layers, and not just in the surface layers most impacted by the irradiation.

3. Discussion and Conclusion

In this paper, we have demonstrated that nanoscale artificial defects (created with FIB irradiation) can be used to nucleate Néel-type, isolated, single skyrmions at precise locations in polycrystalline magnetic multilayer systems at room temperature in low, even zero, applied magnetic field. We have studied this effect in different multilayer systems and draw two interesting conclusions. First, in samples that are known to support skyrmions, the defects create an additional pocket of skyrmion stability at a lower applied field strength than without artificial defects. In sample 1 as-grown, skyrmions are observed between -50 and -80 mT but with defects skyrmions are also stable between $+15$ and -5 mT. Second, as observed in sample 2, these artificial defects can even stabilize skyrmions in samples with lower DMI strength that naturally support homochiral Néel walls but never stabilize skyrmions on field cycling alone.

The mobility of these FIB nucleated skyrmions remains to be studied. The structural imaging of the defects, **Figure 2**, indicates that nucleation is most successful at defects with

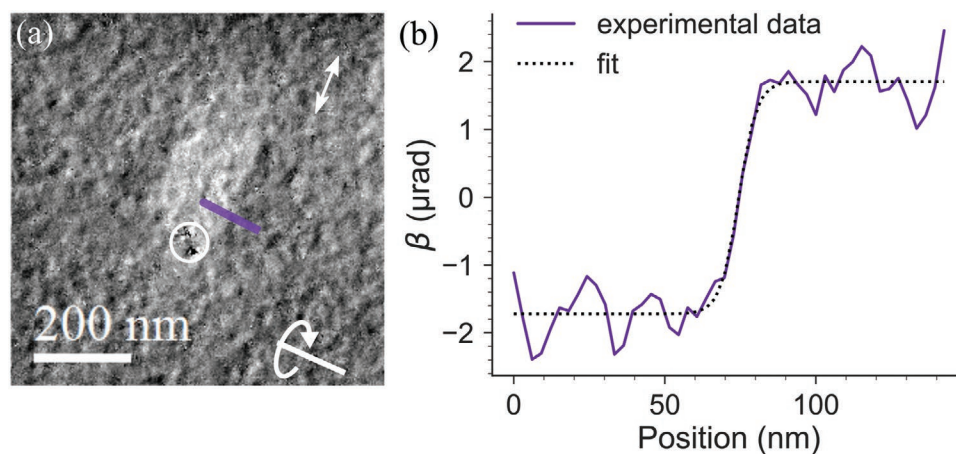


Figure 5. a) DPC image of sample 1, tilted by $\approx 25^\circ$ about the axis indicated, with a 150 nm skyrmion nucleated at a 5×10^{16} ions per cm^2 defect site. The component of magnetic induction mapped is indicated by the double-headed arrow inset top left. The circle gives the size and position of the defect and the line shows where the line trace b)—averaged over 15 lines—was taken.

partial layer intermixing—undoubtedly this intermixing is associated with local lowering of the perpendicular anisotropy and DMI strength as both originate from the layer interfaces. Both of these effects will likely increase the depinning field, as will the local reduction in M_s predicted by alloying.^[23,52]

We note that the size of the skyrmions nucleated appears uninfluenced by the defect itself so long as it is smaller than the inherent skyrmion size. The skyrmion size in a multilayer system is determined by the interplay of various magnetic energy terms controlled by: the strength of the DMI, the anisotropy, the exchange stiffness and the saturation magnetization of the material.^[17] Hence, even though the skyrmions observed in this study are on the order of 100 nm, we expect this nucleation method to successfully nucleate technologically relevant sub-100 nm skyrmions in an optimized material system. To this end we note that it is possible to create smaller FIB defect sites; for example, here we used a 30 keV, 10 pA focused Ga⁺ beam which has a beam diameter of ≈10 nm but a 35 keV, 10 pA focused He⁺ beam has a beam diameter an order of magnitude smaller and can mill sub-10 nm features.^[53,54]

It is expected that new device technologies are more likely to be utilized if they mold into current fabrication methods. A relevant example is that, to support skyrmions, polycrystalline systems are desirable over single crystal systems as they fit with current deposition technologies. Focused ion beam microscopes are widely used in device fabrication (for example in fabrication of semiconductor devices and disk read/write heads) hence controlled skyrmion nucleation at artificial FIB defects is certainly a promising mechanism for reproducible generation of room-temperature, zero-field skyrmions.

4. Experimental Section

Sample Preparation: Sample 1 was prepared at the University of Leeds by dc magnetron sputtering using a base pressure of 2×10^{-8} mbar and an Ar pressure of 6.7 mbar during deposition. Sample 2 was prepared at CNRS/Thalés by dc magnetron sputtering using a base pressure of 8×10^{-8} mbar and an Ar pressure during deposition of 2.5×10^{-3} mbar. Both samples were deposited on top of Pt buffers to control the perpendicular magnetic anisotropy and were capped with Pt to prevent oxidation. Magnetic characterization of the samples prior to defect formation was done using SQUID and AGFM. Artificial defects were created using a FEI Nova NanoLab 200 SEM and FIB using a 30 kV Ga⁺ beam energy and 10 pA current. The patterning method used to fabricate the defects is discussed in detail in the Supporting Information. The cross-sectional lamella was fabricated (from an area containing premade artificial defects) using a standard procedure on a FEI Helios SEM and FIB using a 30 kV Xe⁺ beam energy before a final polish was performed with a 5 kV beam energy.

TEM Imaging: All TEM imaging was performed on a JEOL ARM 200cF equipped with a cold field emission gun and CEOS probe aberration corrector. The HAADF images were collected in “objective on” mode using spot size 5, a 40 μm condenser 1 aperture (convergence angle 36 mrad) and a 2 cm camera length. These conditions give a probe size of <0.2 nm and the HAADF images presented in this paper have a sampling pixel size of 0.2 nm. For the Lorentz TEM images microscope was operated in “objective-off” mode. The Fresnel images were taken with the instrument in TEM mode with a defocus between 5 and 10 μm. The DPC images were taken with the instrument in STEM mode. The DPC dataset was collected using the Medipix3 hybrid pixelated detector with a Merlin readout system. The DPC image shown in this paper was taken

using spot size 1, a 20 μm condenser 1 aperture (convergence angle 1 mrad) and a 1500 cm camera length. This gave a probe size of 3 nm and, in the DPC image presented, the sampling pixel size was 3 nm.

Data Availability: Data associated with this work is available from the University of Glasgow: Enlighten Data repository under a CC-BY license at <http://dx.doi.org/10.5525/gla.researchdata.893>.

Supporting Information

Supporting Information is available from the Wiley Online Library or from the author.

Acknowledgements

The authors acknowledge financial support from European Union grant MAGicSky No. FETOpen-665095; and from the EPSRC through grants EP/M024423/1 and EP/P001483/1; and from the Agence Nationale de la Recherche, France, under Grant Agreement No. ANR-17-CE24-0025 (TOPSKY).

Conflict of Interest

The authors declare no conflict of interest.

Keywords

ion irradiation, magnetic multilayers, magnetic skyrmions, skyrmion nucleation

Received: December 19, 2019

Revised: February 14, 2020

Published online: March 5, 2020

- [1] I. Dzyaloshinsky, *J. Phys. Chem. Solids* **1958**, *4*, 241.
- [2] T. Moriya, *Phys. Rev.* **1960**, *120*, 91.
- [3] S. Mühlbauer, B. Binz, F. Jonietz, C. Pfleiderer, A. Rosch, A. Neubauer, R. Georgii, P. Böni, *Science* **2009**, *323*, 915.
- [4] X. Z. Yu, Y. Onose, N. Kanazawa, J. H. Park, J. H. Han, Y. Matsui, N. Nagaosa, Y. Tokura, *Nature* **2010**, *465*, 901.
- [5] X. Z. Yu, N. Kanazawa, W. Z. Zhang, T. Nagai, T. Hara, K. Kimoto, Y. Matsui, Y. Onose, Y. Tokura, *Nat. Commun.* **2012**, *3*, 988.
- [6] F. Jonietz, S. Mühlbauer, C. Pfleiderer, A. Neubauer, W. Münzer, A. Bauer, T. Adams, R. Georgii, P. Böni, R. A. Duine, K. Everschor, M. Garst, A. Rosch, *Science* **2010**, *330*, 1648.
- [7] M. Bode, M. Heide, K. Von Bergmann, P. Ferriani, S. Heinze, G. Bihlmayer, A. Kubetzka, O. Pietzsch, S. Blügel, R. Wiesendanger, *Nature* **2007**, *447*, 190.
- [8] S. Heinze, K. Von Bergmann, M. Menzel, J. Brede, A. Kubetzka, R. Wiesendanger, G. Bihlmayer, S. Blügel, *Nat. Phys.* **2011**, *7*, 713.
- [9] A. Fert, N. Reyren, V. Cros, *Nat. Rev. Mater.* **2017**, *2*, 17031.
- [10] N. Romming, C. Hanneken, M. Menzel, J. E. Bickel, B. Wolter, K. Bergmann, A. Kubetzka, R. Wiesendanger, *Science* **2013**, *341*, 636.
- [11] A. Hrabec, N. A. Porter, A. Wells, M. J. Benitez, G. Burnell, S. McVitie, D. McGrouther, T. A. Moore, C. H. Marrows, *Phys. Rev. B* **2014**, *90*, 020402.
- [12] C. Moreau-Luchaire, S. C. Mouta, N. Reyren, J. Sampaio, C. A. Vaz, N. Van Horne, K. Bouzehouane, K. Garcia, C. Deranlot, P. Warnicke, P. Wohlhüter, J. M. George, M. Weigand, J. Raabe, V. Cros, A. Fert, *Nat. Nanotechnol.* **2016**, *11*, 444.

- [13] K. Zeissler, M. Mruczkiewicz, S. Finizio, J. Raabe, P. M. Shepley, A. V. Sadovnikov, S. A. Nikitov, K. Fallon, S. McFadzean, S. McVitie, T. A. Moore, G. Burnell, C. H. Marrows, *Sci. Rep.* **2017**, *7*, 15125.
- [14] A. Soumyanarayanan, M. Raju, A. L. Oyarce, A. K. Tan, M. Y. Im, A. P. Petrovic, P. Ho, K. H. Khoo, M. Tran, C. K. Gan, F. Ernult, C. Panagopoulos, *Nat. Mater.* **2017**, *16*, 898.
- [15] S. Woo, K. Litzius, B. Krüger, M. Y. Im, L. Caretta, K. Richter, M. Mann, A. Krone, R. M. Reeve, M. Weigand, P. Agrawal, *Nat. Mater.* **2016**, *15*, 501.
- [16] G. Yu, P. Upadhyaya, X. Li, W. Li, S. K. Kim, Y. Fan, K. L. Wong, Y. Tserkovnyak, P. K. Amiri, K. L. Wang, *Nano Lett.* **2016**, *16*, 1981.
- [17] O. Boulle, J. Vogel, H. Yang, S. Pizzini, D. de Souza Chaves, A. Locatelli, T. O. Menteş, A. Sala, L. D. Buda-Prejbeanu, O. Klein, M. Belmeguenai, *Nat. Nanotechnol.* **2016**, *11*, 449.
- [18] K. Zeissler, S. Finizio, K. Shahbazi, J. Massey, F. A. Ma'Mari, D. M. Bracher, A. Kleibert, M. C. Rosamond, E. H. Linfield, T. A. Moore, J. Raabe, G. Burnell, C. H. Marrows, *Nat. Nanotechnol.* **2018**, *13*, 1161.
- [19] J. Sampaio, V. Cros, S. Rohart, A. Thiaville, A. Fert, *Nat. Nanotechnol.* **2013**, *8*, 839.
- [20] J. Iwasaki, M. Mochizuki, N. Nagaosa, *Nat. Nanotechnol.* **2013**, *8*, 742.
- [21] W. Jiang, P. Upadhyaya, W. Zhang, G. Yu, M. B. Jungfleisch, S. G. E. Velthuis, A. Hoffmann, *Science* **2015**, *349*, 283.
- [22] A. Hrabec, J. Sampaio, M. Belmeguenai, I. Gross, R. Weil, S. M. Cherif, A. Stashkevich, V. Jacques, A. Thiaville, S. Rohart, *Nat. Commun.* **2017**, *8*, 15765.
- [23] W. Legrand, D. Maccariello, N. Reyren, K. Garcia, C. Moutafis, C. Moreau-Luchaire, S. Collin, K. Bouzehouane, V. Cros, A. Fert, *Nano Lett.* **2017**, *17*, 2703.
- [24] S. Finizio, K. Zeissler, S. Wintz, S. Mayr, T. Weißels, A. J. Huxtable, G. Burnell, C. H. Marrows, J. Raabe, *Nano Lett.* **2019**, *19*, 7246.
- [25] T. Ogasawara, N. Iwata, Y. Murakami, H. Okamoto, Y. Tokura, *Appl. Phys. Lett.* **2009**, *94*, 162507.
- [26] M. Finazzi, M. Savoini, A. R. Khorsand, A. Tsukamoto, A. Itoh, L. D'ùo, A. Kirilyuk, T. Rasing, M. Ezawa, *Phys. Rev. Lett.* **2013**, *110*, 177205.
- [27] S. G. Je, P. Vallobra, T. Srivastava, J. C. Rojas-Sánchez, T. H. Pham, M. Hehn, G. Malinowski, C. Baraduc, S. Auffret, G. Gaudin, S. Mangin, H. Béa, O. Boulle, *Nano Lett.* **2018**, *18*, 7362.
- [28] P. J. Hsu, A. Kubetzka, A. Finco, N. Romming, K. Von Bergmann, R. Wiesendanger, *Nat. Nanotechnol.* **2017**, *12*, 123.
- [29] T. Srivastava, M. Schott, R. Juge, V. Křížáková, M. Belmeguenai, Y. Roussigné, A. Bernand-Mantel, L. Ranno, S. Pizzini, S. M. Chérif, A. Stashkevich, *Nano Lett.* **2018**, *18*, 4871.
- [30] F. Büttner, I. Lemesch, M. Schneider, B. Pfau, C. M. Günther, P. Hessian, J. Geilhufe, L. Caretta, D. Engel, B. Krüger, J. Viehhaus, S. Eisebitt, G. S. Beach, *Nat. Nanotechnol.* **2017**, *12*, 1040.
- [31] S. Woo, Y. Zhou, K. M. Song, B.-C. Min, J. Raabe, X. Zhang, K.-Y. Lee, J. Chang, X. Liu, M.-C. Park, M. Weigand, M. Ezawa, J. W. Choi, S. Finizio, H. C. Koo, *Nat. Electron.* **2018**, *1*, 288.
- [32] V. M. Uzdin, M. N. Potkina, I. S. Lobanov, P. F. Bessarab, H. Jónsson, *Phys. B* **2018**, *549*, 6.
- [33] L. Desplat, D. Suess, J.-V. Kim, R. L. Stamps, *Phys. Rev. B* **2018**, *98*, 134407.
- [34] C. Chappert, H. Bernas, J. Ferré, V. Kottler, J.-P. Jamet, Y. Chen, E. Cambril, T. Devolder, F. Rousseaux, V. Mathet, H. Launois, *Science* **1998**, *280*, 1919.
- [35] C. T. Rettner, S. Anders, J. E. Baglin, T. Thomson, B. D. Terris, *Appl. Phys. Lett.* **2002**, *80*, 279.
- [36] C. Vieu, J. Gierak, H. Launois, T. Aign, P. Meyer, J. P. Jamet, J. Ferré, C. Chappert, T. Devolder, V. Mathet, H. Bernas, *J. Appl. Phys.* **2002**, *91*, 3103.
- [37] G. Kusinski, G. Thomas, *Microsc. Microanal.* **2002**, *8*, 319.
- [38] J. Fassbender, D. Ravelosona, Y. Samson, *J. Phys. D: Appl. Phys.* **2004**, *37*, R179.
- [39] A. Aziz, S. J. Bending, H. G. Roberts, S. Crampin, P. J. Heard, C. H. Marrows, *Phys. Rev. Lett.* **2006**, *97*, 206602.
- [40] M. J. Benitez, M. A. Basith, R. J. Lamb, D. McGrouther, S. McFadzean, D. A. MacLaren, A. Hrabec, C. H. Marrows, S. McVitie, *Phys. Rev. Appl.* **2015**, *3*, 034008.
- [41] S. Zhang, A. K. Petford-Long, C. Phatak, *Sci. Rep.* **2016**, *6*, 31248.
- [42] G. H. O. Daalderop, P. J. Kelly, M. F. H. Schuurmans, *Phys. Rev. B* **1994**, *50*, 9989.
- [43] S. McVitie, D. McGrouther, S. McFadzean, D. A. MacLaren, K. J. O. Shea, M. J. Benitez, *Ultramicroscopy* **2015**, *152*, 57.
- [44] M. Krajinak, D. McGrouther, D. Maneuski, V. O. Shea, S. McVitie, *Ultramicroscopy* **2016**, *165*, 42.
- [45] S. McVitie, S. Hughes, K. Fallon, S. McFadzean, D. McGrouther, M. Krajinak, W. Legrand, D. Maccariello, S. Collin, K. Garcia, N. Reyren, V. Cros, A. Fert, K. Zeissler, C. H. Marrows, *Sci. Rep.* **2018**, *8*, 5703.
- [46] K. Fallon, S. McVitie, W. Legrand, F. Ajejas, D. Maccariello, S. Collin, V. Cros, N. Reyren, *Phys. Rev. B* **2019**, *100*, 214431.
- [47] M. J. Benitez, A. Hrabec, A. P. Mihai, T. A. Moore, G. Burnell, D. McGrouther, C. H. Marrows, S. McVitie, *Nat. Commun.* **2015**, *6*, 8957.
- [48] A. Bogdanov, A. Hubert, *Phys. Status Solidi B* **1994**, *186*, 527.
- [49] A. O. Leonov, T. L. Monchesky, N. Romming, A. Kubetzka, A. N. Bogdanov, R. Wiesendanger, *New J. Phys.* **2016**, *18*, 065003.
- [50] N. Romming, A. Kubetzka, C. Hanneken, K. von Bergmann, R. Wiesendanger, *Phys. Rev. Lett.* **2015**, *114*, 177203.
- [51] C. M. Park, J. A. Bain, *J. Appl. Phys.* **2002**, *91*, 6830.
- [52] J. Crangle, D. Parsons, *Proc. of the Royal Society of London. Series A, Mathematical and Physical Sciences*, Vol. 255, The Royal Society, London, **1960**, p. 509.
- [53] N. Bassim, K. Scott, L. A. Giannuzzi, *MRS Bull.* **2014**, *39*, 317.
- [54] G. Hlawacek, V. Veligura, R. van Gastel, B. Poelsema, *J. Vac. Sci. Technol., B: Nanotechnol. Microelectron.: Mater., Process., Meas., Phenom.* **2014**, *32*, 020801.